Acta Biomaterialia 151 (2022) 446–456

Contents lists available at ScienceDirect

Acta Biomaterialia

journal homepage: www.elsevier.com/locate/actbio

Full length article

Crystal orientation mapping and microindentation reveal anisotropy in *Porites* skeletons

Molly A. Moynihan[a,b,*], Shahrouz Amini[c,d], Jeffrey Oalmann[e], J.Q. Isaiah Chua[c], Jani T.I. Tanzil[e,f], T.Y. Fan[g], Ali Miserez[c,h], Nathalie F. Goodkin[e,i]

[a] Earth Observatory of Singapore, Interdisciplinary Graduate School, Nanyang Technological University, Singapore, Singapore
[b] Asian School of the Environment, Nanyang Technological University, Singapore, Singapore
[c] Center for Biomimetic Sensor Science, School of Materials Science & Engineering, Nanyang Technological University, Singapore, Singapore
[d] Max Planck Institute of Colloids and Interfaces, Department of Biomaterials, Potsdam, Germany
[e] Earth Observatory of Singapore, Nanyang Technological University, Singapore, Singapore
[f] St. John's Island National Marine Laboratory, Tropical Marine Science Institute, National University of Singapore, 18 Kent Ridge Road, 119227, Singapore
[g] National Museum of Marine Biology and Aquarium, Pingtung, Taiwan
[h] School of Biological Sciences, Nanyang Technological University, Singapore, Singapore
[i] American Museum of Natural History, New York, NY, USA

ARTICLE INFO

Article history:
Received 9 March 2022
Revised 3 August 2022
Accepted 5 August 2022
Available online 11 August 2022

Keywords:
Corals
Crystal orientation
Biomineralization
Mechanical properties
Microstructure
Indentation
Young's modulus

ABSTRACT

Structures made by scleractinian corals support diverse ocean ecosystems. Despite the importance of coral skeletons and their predicted vulnerability to climate change, few studies have examined the mechanical and crystallographic properties of coral skeletons at the micro- and nano-scales. Here, we investigated the interplay of crystallographic and microarchitectural organization with mechanical anisotropy within *Porites* skeletons by measuring Young's modulus and hardness along surfaces transverse and longitudinal to the primary coral growth direction. We observed micro-scale anisotropy, where the transverse surface had greater Young's modulus and hardness by $\sim$ 6 GPa and 0.2 GPa, respectively. Electron backscatter diffraction (EBSD) revealed that this surface also had a higher percentage of crystals oriented with the a-axis between $\pm$ 30–60°, relative to the longitudinal surface, and a broader grain size distribution. Within a region containing a sharp microscale gradient in Young's modulus, nanoscale indentation mapping, energy dispersive spectroscopy (EDS), EBSD, and Raman crystallography were performed. A correlative trend showed higher Young's modulus and hardness in regions with individual crystal bases (c-axis) facing upward, and in crystal fibers relative to centers of calcification. These relationships highlight the difference in mechanical properties between scales (i.e. crystals, crystal bundles, grains). Observations of crystal orientation and mechanical properties suggest that anisotropy is driven by microscale organization and crystal packing rather than intrinsic crystal anisotropy. In comparison with previous observations of nanoscale isotropy in corals, our results illustrate the role of hierarchical architecture in coral skeletons and the influence of biotic and abiotic factors on mechanical properties at different scales.

Statement of significance

Coral biomineralization and the ability of corals' skeletal structure to withstand biotic and abiotic forces underpins the success of reef ecosystems. At the microscale, we show increased skeletal stiffness and hardness perpendicular to the coral growth direction. By comparing nano- and micro-scale indentation results, we also reveal an effect of hierarchical architecture on the mechanical properties of coral skeletons and hypothesize that crystal packing and orientation result in microscale anisotropy. In contrast to previous findings, we demonstrate that mechanical and crystallographic properties of coral skeletons can vary between surface planes, within surface planes, and at different analytical scales. These results im-

* Corresponding author. Present address: Marine Biological Laboratory, Woods Hole, MA, USA.
E-mail addresses: mmoynihan@mbl.edu, moyn0001@e.ntu.edu.sg (M.A. Moynihan).

https://doi.org/10.1016/j.actbio.2022.08.012
1742-7061/© 2022 The Author(s). Published by Elsevier Ltd on behalf of Acta Materialia Inc. This is an open access article under the CC BY-NC-ND license (http://creativecommons.org/licenses/by-nc-nd/4.0/)

prove our understanding of biomineralization and the effects of scale and direction on how biomineral structures respond to environmental stimuli.

© 2022 The Author(s). Published by Elsevier Ltd on behalf of Acta Materialia Inc.
This is an open access article under the CC BY-NC-ND license
(http://creativecommons.org/licenses/by-nc-nd/4.0/)

1. Introduction

Corals, a key structural component in reef environments, are among the fastest calcifying marine organisms [1–3]. Coral skeletons provide critical habitat, supporting marine biodiversity, and also form the primary substrate of reef platforms [3–6]. During biomineralization, corals precipitate calcium carbonate extracellularly in the form of orthorhombic aragonite crystals [7]. The skeletal ultra-structure consists of two components, centers of calcification (COCs) (a.k.a rapid accretion deposits) and fibers (a.k.a thickening deposits) [2,7,8]. Although precipitation occurs simultaneously in both regions [8–11], COCs and fibers have different nanostructural organizations and heterogenous growth rates [12,13]. COCs are composed of nanometer aragonite globules with a higher content of organic molecules and amorphous calcium carbonate [1,13–15]. Fibers consist of bundles of aragonite crystals in grains of crystallographic continuity arranged in fan-like bundles around COCs, forming plumose spherulites [15,16]. Skeletal fibers compete for space and display a wide range of crystallographic orientations [16,17]. This high space filling rate has been hypothesized as an evolutionary mechanism to increase the ability of aragonite to withstand mechanical deformation [16].

The ability of coral skeletons to withstand mechanical deformation is important for reef health and ecosystem functioning [18–20]. However, the majority of mechanical deformation studies on coral skeletons have employed bulk-scale measurements of structural properties (e.g density, porosity, breaking strength) [19–22]. In contrast, micro- and nano-scale measurements of coral mechanical properties can tell us how resistant the skeletal material is to deformation [23] while also providing insight into crystal organization and composition, which may ultimately drive changes in mechanical deformation [16]. Yet, despite widespread studies of coral biomineralization, the mechanical properties of coral skeletons have rarely been studied at the micro- and nano-scale [24,25]. Recent studies have attributed rapid calcification rates in coral to crystal organization patterns [16]; however, no study has directly compared patterns of crystal organization with micro-scale mechanical measurements. We hypothesize that multi-length scale indentation measurements, in which the mechanical response of the individual crystals and crystal bundles can be probed, can disentangle the mechanical characteristics of the individual crystallites from bundle crystals and clarify the role of microarchitectural arrangement of crystallite packing on the mechanical performance of the corals.

Young's modulus and hardness are two principal mechanical properties that can be measured using depth sensing nanoindentation. Young's modulus is a measure of resistance to elastic deformation, and hardness is a measure of resistance to inelastic deformation induced by compression forces. In contrast to conventional Vickers hardness, which has also been measured in coral skeletons [26], nanoindentation hardness uses smaller loads and forms minute tip-sample interaction volumes, providing location-specific mechanical information with submicron spatial resolution, resulting in more accurate ultrastructure-property interrelationships. Materials that have the same properties when measured in different directions are *isotropic*, and those with different properties when measured in different directions are *anisotropic*. Biological materials often possess hierarchical architectures resulting in superior mechanical properties, which frequently surpass those of their basic constituents. Given differences in skeletal architecture between coral species and morphologies, hierarchical architecture may also result in organismal-level differences in mechanical properties between corals. Moreover, the presence of hierarchical architectures inevitably induces anisotropies and heterogeneities in mechanical properties.

Bulk-scale studies have reported anisotropic properties in coral skeletons, with compressive strength varying along transverse and longitudinal axes of branching coral [20,21]. Significant differences in compressive strength were also observed between branching and massive morphologies [19–21]. In contrast, studies of coral samples from the Mediterranean and Red Sea found that micromechanical properties (e.g. Young's modulus) were isotropic and constant between species [25]. Studies of crystal orientation using applied atomic force microscopy and X-ray diffraction (XRD) also found no preferred orientation of *Stylophora pistillata* and *Balanophyllia europaea* [25]. However, biogenic aragonite is anisotropic by nature [27–29], and anisotropy has been documented in coral aragonite crystals across a range of environments [30]. The wide range of crystallographic orientations observed in coral skeletons, driven by spherulitic growth, is hypothesized to result in isotropic properties at the micromechanical scale [16]. Yet, the spatial resolution of XRD analysis is limited in comparison with micromechanical measurements, and to date, paired high resolution crystal orientation mapping and micromechanical measurements have yet to be performed in tropical scleractinian corals. Due to difficulties in obtaining crystal orientation data in carbonate samples, such data is generally lacking in the literature and limited to small areal measurements [16,17,22,24,31], with only one study mapping a continuous area greater than 0.07 mm^2, in the slow-growing and azooxanthellate cold-water coral *Lophelia pertusa* [32]. Work combining crystal orientation mapping and bulk scale mechanical measurements has revealed that both crystal fiber organization and breaking strength can decrease as a result of ocean acidification [22]. Such studies highlight the need for paired crystallographic and finer scale micro- and nano- mechanical data.

To address these knowledge gaps, this study combines mechanical measurements (micro- and nano-indentation) of *Porites* skeletons with high-resolution crystal orientation mapping. We test the assumption that coral skeletons are isotropic, as previously documented [25], and perform repeated measurements along growth axes and between cores, to test the robustness of observed trends. Along regions with sharp gradients in microscale mechanical properties, we then map Young's modulus and hardness at a higher spatial resolution, and compare these nanoscale mechanical properties with crystal orientation from both electron backscatter diffraction (EBSD) and Raman spectroscopy, as well as mineral composition using Energy-Dispersive X-ray Spectroscopy (EDS). By comparing crystal orientation with nanoindentation, we directly test the hypothesis that spherulitic growth enhances skeletal mechanical properties. These findings offer insight into the hierarchical architecture and biomineralization patterns of *Porites* skeletons, which are important contributors to reef structure and substrate [4,33] and are widely used in geochemical, biological, and ecological studies of tropical reefs.

2. Materials & methods

2.1. Sample collection and preparation

Coral samples used in this study were from massive *Porites* cores collected in Hengchun, Taiwan: Wanlitung (21.97° N, 120.71° E) (WLT) and Houbihu (21.94° N, 120.75° E) (HBH), approximately 7km apart. WLT and HBH were both cored using a hydraulic drill at depths of 3 m and 5 m, respectively. An additional core (KRD) from Phuket, Thailand (7.6131° N, 98.3728° E) was used to validate trends in WLT. Core collection is detailed in [23]. Coral slabs were immersed in sodium hypochlorite shortly after collection. From each coral core, small fragments were cut below the tissue layer, cleaned with ultra-sonication, and embedded in epoxy resin. Cold mounting epoxy resin (EpoFix, Struers) was used to avoid any alteration of the intracrystalline skeletal organic components, and samples were cured under low-vacuum allowing the resin to infuse only into large cavities while avoiding the skeletal ultrastructure. Absence of resin inside the skeletal ultrastructure, including the COCs, was verified using collected Raman spectra (see below) (Fig. S1). Embedded samples were polished with sand paper of decreasing mesh size (1000 down to 4000 grit) and finally with a colloidal silica suspension (particle size 40 nm) (Struers), followed by ultrasonication. The WLT sample was polished to expose three faces of a single corallite: 1 transverse surface (surface 1; perpendicular to the primary vertical growth direction) and 2 longitudinal surfaces (surfaces 2 & 3; parallel to the primary vertical growth direction) (Fig. 1). HBH was only polished to expose the longitudinal surface (surface 2).

2.2. Indentation

Indentation measurements were performed using a TI 950 TriboIndenter (Bruker-Hysitron, MN, USA) equipped with a 2D standard transducer (10mN max force). To evaluate the mechanical anisotropy, directional robustness, and heterogeneities in our coral samples, a series of three indentation experiments were designed and performed. On surface 1 (transverse) the direction of force applied during indentation was parallel to the primary macroscale vertical growth direction, whereas on surfaces 2 & 3 (longitudinal), the direction of force applied was perpendicular to this growth direction.

Microindentation – (i) To study the micromechanical anisotropy of the samples in x, y, and z planes (surfaces 1–3) (Fig. 1) within a single corallite, a cono-spherical indenter with a tip radius of 5 μm was used. The cono-spherical tip (rather than a sharp and pyramid-shaped tip) postpones inelastic damages and cracking events, resulting in a more precise measurement of elastic modulus [23,34]. To avoid surface defects (e.g., scratches, porosities, etc), the indentation locations were analysed by scanning probe microscopy (SPM) prior to the nanoindentation measurement. For the measurements, a maximum load of 10 mN and a load function of 5s loading - 2s holding - 5s unloading were used. Areas of 60 μm × 60 μm were probed in grids of 20 indents, with indents separated by 10 μm. These measurements were performed within a single corallite on three surfaces of the Taiwan WLT core and on two surfaces of the Thailand KRD core, for verification that anisotropy was not specific to a given corallite, coral, or location. (ii) To test for the robustness of directional measurements across different microscale features, indentation was performed twice along surface 2 of HBH, once after re-polishing and exposing a different set of crystals. When repeating indentation along the re-polished core, measurements were performed at similar depths within the coral core (i.e. deposited at a similar time along the same surface), but at random positions within a given depth of the core. Repeated measurements spanned four years of growth. A cono-spherical tip was used, as described above.

Nanoindentation – (iii) To investigate the heterogeneities of nanomechanical properties and possible correlations with the crystallographic orientation of the aragonite crystals, high-resolution indentation mapping was done using a Berkovich indenter (tip radius of 140 nm), which can provide a higher spatial resolution in comparison with cono-spherical tips. A maximum load of 4 mN, a load function of 5s loading - 2s holding - 5s unloading and spacing of 5 μm was used to probe an area of 110 μm × 220 μm.

For all measurements, the tip areas were calibrated using standard fused quartz and aluminium samples for the required contact depths. Hardness was determined by the maximum load divided by the contact area, and Young's modulus was determined using the Oliver and Pharr [35] method. Indents that displayed severe pop-in events due to micro-cracking around the indents were discarded from Young's modulus and hardness calculations.

2.3. Crystal orientation and elemental mapping

A JEOL JSM-7800F field emission scanning electron microscope (FESEM), equipped with an electron back scatter diffraction (EBSD) detector (Oxford NordlysNano) and two energy dispersive x-ray spectrometers (EDS) (Oxford X-Max 150 mm^2), was used to image samples and to determine both crystal orientation (EBSD) and mineral composition (EDS). EBSD determines the orientation of solid crystals using diffraction patterns, known as Kikuchi patterns, which are generated by interactions between the electron beam and the crystal lattice. EDS determines the elemental composition of the skeleton, as minerals emit characteristic X-rays after being excited by an electron beam.

For EBSD measurements and EDS mapping, the system was operated in low vacuum mode with a 3.1 nA probe current and 15 kV accelerating voltage. For EBSD, a 18.7 mm working distance was used, step-size ranged from 0.5–1.5 mm and exposure time from 82 to 246 ms, depending on the scan area. Binning mode was set to 1 × 1, with a frame average of 1 and low gain. EDS mapping was performed at 10 mm working distance, using 1024 pixels per frame and 500 ms pixel dwell time. For FESEM imaging in Fig. 1, samples were etched in 0.1% formic acid for 45 s [36,37]. Prior to EBSD, EDS, and Raman spectroscopy analysis (details below), samples were polished with decreasing mesh size (1000 down to 4000 grit) followed by a colloidal silica suspension (particle size 40 nm) (Struers) and ultrasonication.

EBSD was performed on all three surfaces of the WLT core and on surface 2 of the HBH core. Due the high variability in Young's modulus observed along surface 2 of the Taiwan HBH core [23], EDS mapping and Raman spectroscopy (details below) were performed on HBH. The MTEX Matlab (R2020a) toolbox was used for EBSD analysis and to determine grain size [38]. Inverse pole figure (IPF) maps display color-coded orientation information using Miller indices ([100], [010]. [001]). The [001] direction is parallel to the morphological axis of the crystal fiber (c-axis). Orientation density functions (ODFs) are used to show the stereographic projection of the (100), (010), (001) and (222) aragonite planes. Note that these planes are not related to indentation surfaces defined in Fig. 1, but rather pertain to the orientation of crystals within grains of a given surface. ODFs reveal both crystallographic orientations and the volume percentage of crystals in specific orientations.

To visualize patterns in crystal orientation, trichromic EBSD maps were generated with orientations binned by ± 0–30°, ± 30–60°, ± 60–90° about the a-axis. The number of pixels corresponding to each color was counted to determine the percent contribution of crystals from each orientation bins (*n* pixels counted per surface: 1 = 2,716,917; 2 = 2,117,117; 3 = 2,518,557).

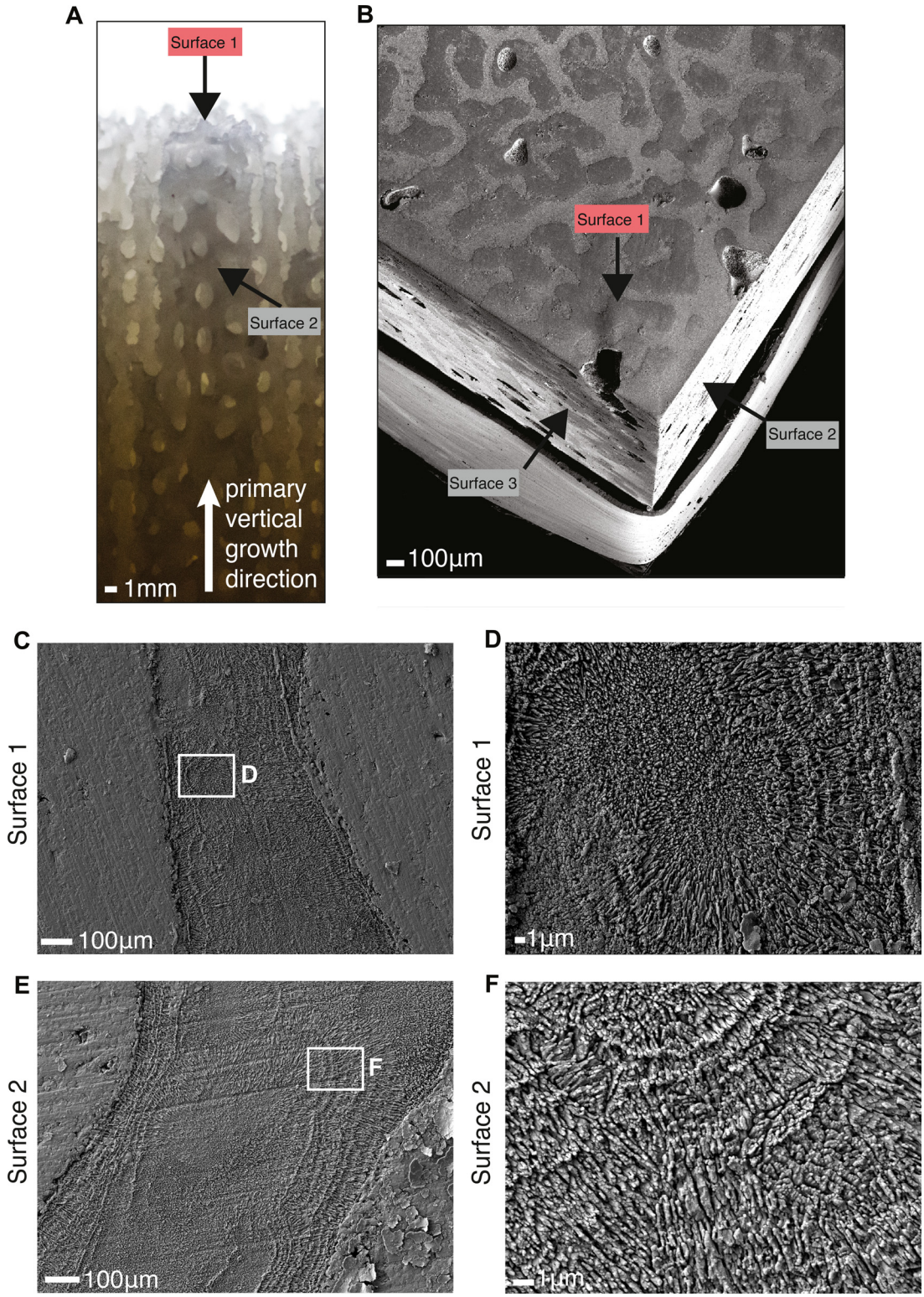

Fig. 1. Micrographs illustrating the coral surfaces analyzed in this study. (A) Optical micrograph of a non-embedded *Porites* skeleton sample showing the direction of analysis for surface 1 and surface 2, with an arrow indicating the primary vertical growth direction at the macroscale. (B) *Porites* skeleton embedded in resin and polished to expose the three perpendicular surfaces: surface 1 (transverse) and surfaces 2 & 3 (longitudinal). Indentation measurements on surface 1 were parallel to the primary vertical growth direction, and indentation measurements on surfaces 2 & 3 were perpendicular to the primary vertical growth direction. Field Emission Scanning Electron Microscope (FESEM) micrographs of (C, D) etched surface 1 and (E,F) surface 2. Note that growth directions within individual fine-scale components (i.e. COCs and fibers) can differ from the primary vertical growth direction.

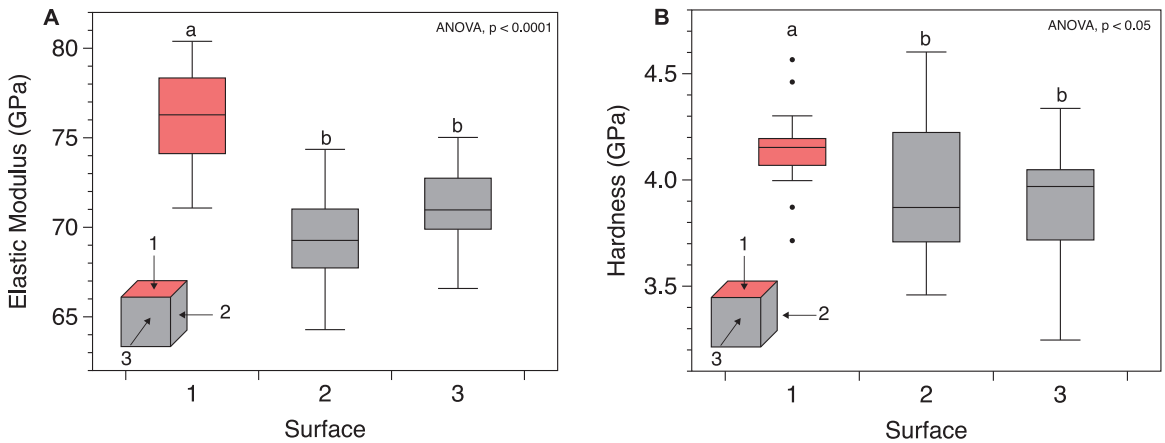

Fig. 2. Micromechanical anisotropy in WLT sample. (A) Young's modulus (GPa) and (B) hardness (GPa) measured using depth-sensing microindentation in surfaces 1 (coral growth direction) ($n = 16$), 2 ($n = 17$), and 3 ($n = 16$) of the WLT Porites sample. Young's modulus and hardness differed between surfaces (ANOVA, $p < 0.05$) and were higher in the primary vertical growth direction (surface 1) than surfaces 2 and 3. Statistically different groupings indicated by a and b.

2.4. Raman crystallography

Polarized Raman spectroscopy was performed on the Taiwan HBH core using a confocal Raman spectroscope (Alpha 300, WITec, Germany) equipped with a 532 nm laser wavelength and 20× magnification objective lens. To obtain the orientation dependent spectral from the samples [39], an analyzer filter at 0° and 90° was used for parallel and cross polarization. Accordingly, all the measurements were done twice to collect the Raman spectra or maps in parallel and cross polarizations. Monocrystal geological aragonite was used as a standard to determine the crystallographic orientation of aragonite. During point measurements of the geological aragonite sample, an integration time of 1 s and an accumulation of 30 were used. For the mapping of the coral sample, an area of 85 μm × 200 μm with a spatial resolution of 1 μm was mapped using an integration time of 5 s. The measurements were done using a 1800 grooves/mm grating, which provides a spectral resolution of 1 cm^{-1} when combined with the 532 nm laser wavelength. WITec Project 5.2 and OriginPro 2020 were used for data analysis and spectra plotting, respectively.

2.5. Data analysis

Data analysis and plotting were done using MTEX [38], R [40], Datagraph, WITec, and OriginPro software. The number of replicates (n) varied by experiment and is listed the respective text. Trichromic EBSD maps were generated in MTEX using groupings of ±0-30°, ±30-60°, ±60-90° relative to the a-axis, and total pixel counts of each color were determined. Associated scripts are provided along with raw data files (see Supplementary Material).

Shapiro-Wilk's test was used to test for normality of nanoindentation data, and the Anderson Darling test was used to test for normality of grain size data, due to the large number of data points. Analysis of Variance (ANOVA) with TukeyHSD post hoc tests and Welch t-tests were used on nanoindentation data. Due to outliers in hardness measurements along surface 1, TukeyHSD post hoc tests determined only nearly statistically significant hardness groupings. Additional testing was performed to show that hardness along surface 2 and surface 3 were not statistically different (t-test, $p > 0.05$) from each other, while surface 1 hardness differed from surfaces 2 and 3 (t-test, $p < 0.05$). An additional nonparametric test less sensitive to outliers (Kruskal-Wallis, Fisher post hoc, Hochberg adjustment) was used to confirm that surface 1 hardness differed significantly from surfaces 2 & 3. A Kruskal-Wallis test (Fisher post hoc, Hochberg adjustment) was used to analyze grain size data between surfaces.

Table 1
Percent contribution of crystals with orientation bins (± 0–30°, ± 30–60°, ± 60–90°) relative to the a-axis in surfaces 1 – 3.

Surface	Percent of a-axis rotational bins		
	± 0–30°	± 30–60°	± 60–90°
Surface 1	40.57%	45.21%	14.23%
Surface 2	46.11%	38.83%	15.06%
Surface 3	43.92%	40.68%	15.40%

3. Results

3.1. Anisotropy, crystal orientation, and grain size between surfaces

Microindentation of three corallite surfaces from Taiwan (WLT) revealed significantly greater Young's modulus and hardness values parallel to the primary macroscale direction of coral growth by approximately 6 GPa (Fig. 2) (ANOVA, $p < 0.0001$) and 0.2 GPa (ANOVA, $p < 0.05$), respectively ($n = 49$). To confirm that this trend was not unique to WLT or a single corallite, additional tests were performed in the KRD core, which also displayed even more pronounced anisotropy, with surface 1 having an average Young's modulus of 81.98 GPa ± 4.91 and the surface 2 Young's modulus was 48.53 ± 3.79 GPa ($n = 20$).

Crystal orientation mapping of the three WLT surfaces were relatively similar (Fig. 3). When grouped by crystallographic angle relative to the a-axis (Fig. 4), patterns in crystallographic orientations were more apparent. Surface 1 had a higher percentage of crystals oriented with the a-axis between ± 30–60°, and surfaces 2 & 3 had a higher percentage of crystals with the a-axis between 0–30° (Table 1). Orientation density functions (ODFs) showed that (001) and (100) planes were more dispersed in surface 2 and surface 3, relative to surface 1 (Fig. 3). Centers of calcification (COCs), also known as rapid accretion deposit areas, were visible as non-indexed areas. These regions did not produce Kikuchi patterns and thus did not index as any crystalline polymorph of calcium carbonate (e.g. aragonite, calcite). In surface 1, COCs were typically surrounded by crystals with the [010] and [100] axis perpendicular to the surface, whereas in surfaces 2 & 3, COCs were predominately surrounded by crystals with the [010] axis perpendicular to the surface.

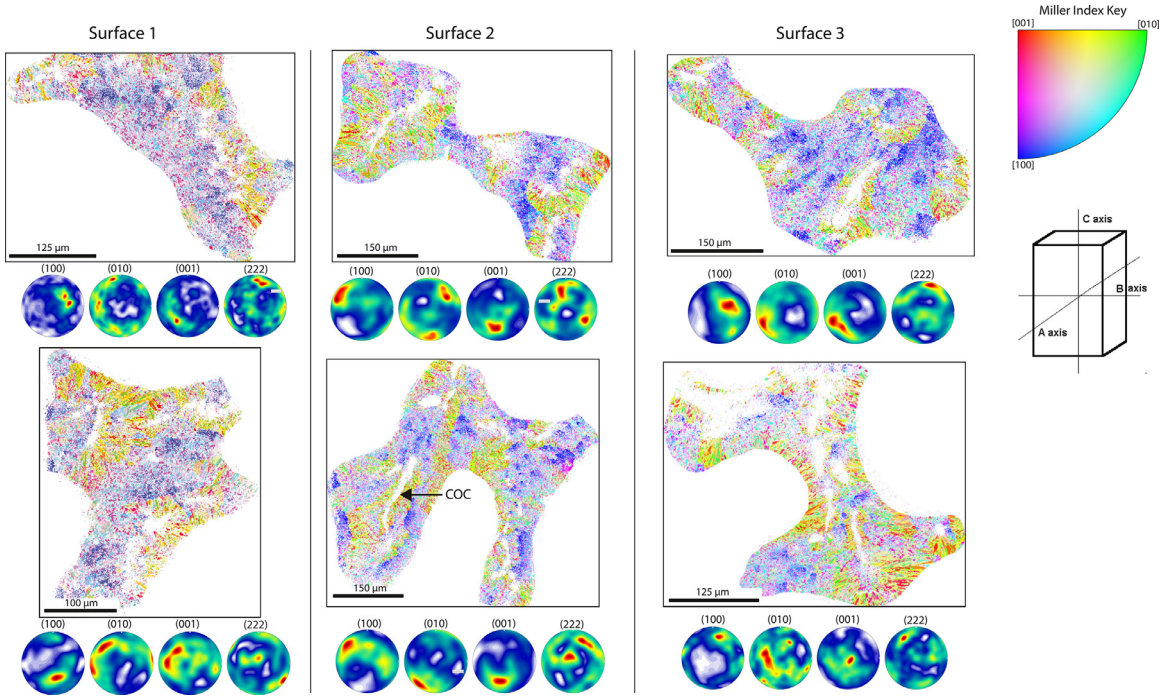

Fig. 3. Inverse pole figures (IPF) and orientation density functions (ODFs) of crystal orientation data from electron backscatter diffraction (EBSD) analysis of surfaces 1 – 3 of the WLT *Porites* sample. Two locations within each surface are displayed in columns. Colors in IPF figures correspond with crystallographic directions (Miller indices) of pixels that are perpendicular to the map surface. ODF plots (spheres) show the density and distribution of orientations within given crystallographic planes (100), (010), (001), and (222). Centers of calcification (COCs) are non-indexed regions surrounded by indexed crystals, and an example COC is demarcated in Surface 2. (For interpretation of the references to colour in this figure legend, the reader is referred to the web version of this article.)

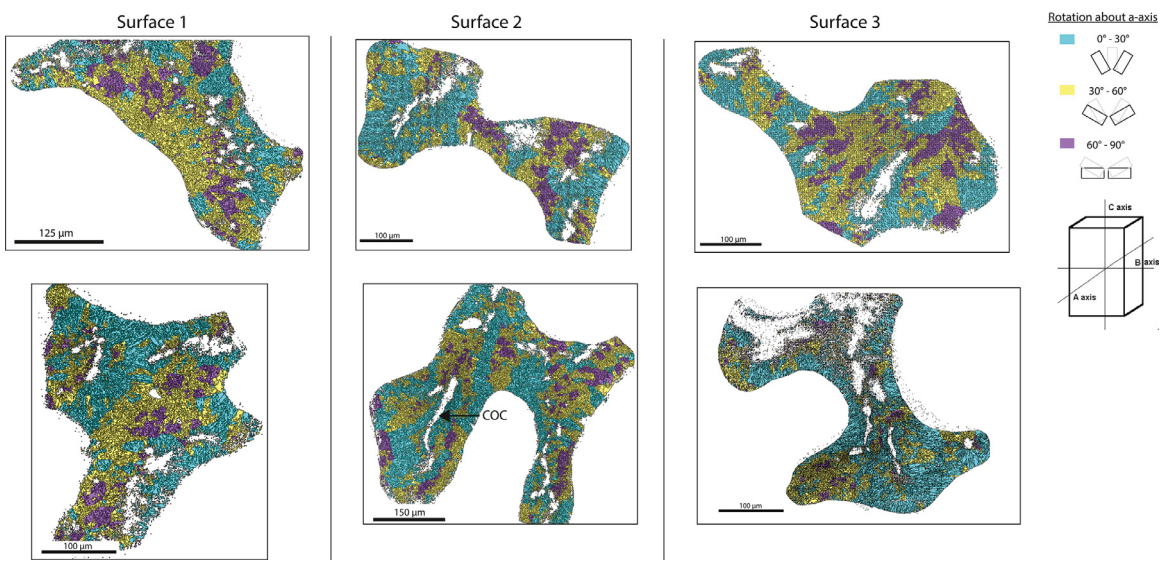

Fig. 4. Trichromic mapping of crystal orientation data from electron backscatter diffraction (EBSD) analysis of surfaces 1 – 3 of the WLT *Porites* sample. Two locations within each surface are displayed in columns. Crystallographic directions were clustered based on their orientation about the a-axis (cyan = 0 – 30°; yellow = 30 – 60°; magenta = 60 – 90°). Centers of calcification (COCs) are non-indexed regions surrounded by indexed crystals, and an example COC is demarcated in Surface 2. (For interpretation of the references to colour in this figure legend, the reader is referred to the web version of this article.)

Grain size measurements from EBSD data using MTEX [38] revealed a variable size, averaging 10.0 ± 12.1 μm^2. Surface 1 had a broader distribution pattern and had significantly higher grain size than surfaces 2 or 3 (Kruskal-Wallis, Fisher post hoc, Hochberg adjustment, $p < 0.001$) (Fig. 5). With an average cono-spherical indentation contact depth of 200 nm, each indent compresses an area of approximately 6 μm^2. In comparison with aragonite crystal diameter ($< 1\mu m$), we estimate that individual indents comprised several tens of crystals from a single grain and indentation grids (2000 μm^2) contained over 100 neighboring grains.

3.2. Chemical composition, crystal orientation, and nanoindentation mapping within a surface

HBH was selected for further mechanical testing and orientation mapping, because its properties were observed to change more drastically on a small spatial scale with depth along the coral core, relative to WLT [23]. Due to the sharp decrease in Young's modulus observed in 2012 – 2011 in the HBH core [23], the sample was polished and indentation measurements were repeated. Re-polishing this surface exposed different crystals, and indent re-

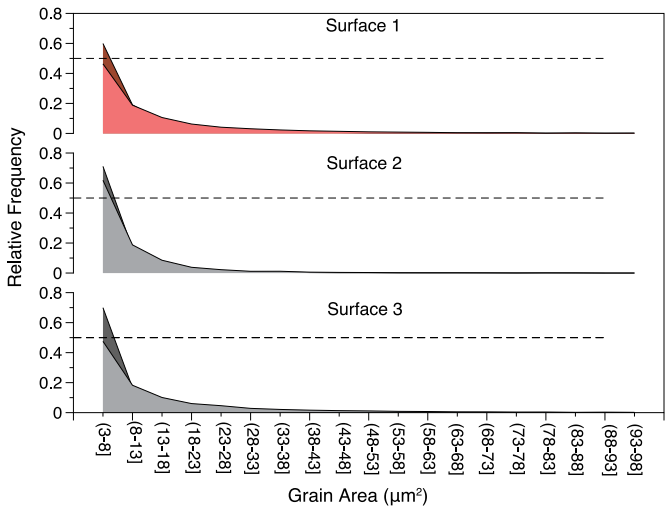

Fig. 5. Grain size (μm^2) relative frequency distribution from surfaces 1 ($n = 13,409$), 2 ($n = 14,547$), 3 ($n = 18,688$) of the WLT *Porites* sample. Grain size was determined from electron backscatter diffraction (EBSD) data. Grain areas are binned by increments of 5 μm^2. All three surfaces had significantly different grain size distributions, with surface 1 having the largest average grain size (Kruskall-Wallis, Fisher post hoc, Hochberg adjustment, $p < 0.001$).

gions were performed within different skeletal features and corallites. Yet, the same trend in Young's modulus was observed on the re-polished track (Fig. 6). This finding suggests that crystals deposited at a similar time along a given surface have preferred microscale mechanical and crystallographic properties, despite the fact that coral growth is heterogeneous. EDS analysis along the region with the sharpest gradient in Young's modulus (2012-2011) revealed no evident trend in mineral composition of atom % C, O, Ca, Mg, Sr, or Ba (only Ca, Mg shown here) (Fig. 6B & C). Within the non-indexed regions, atom % Ca appeared higher and atom % Mg lower, relative to the surrounding crystals. However, electron micrographs reveal that this region may be less smooth than the surrounding region (Fig. 7C), likely due to its amorphous phase or higher porosity, causing it to damage more easily during polishing. This would result in a rough surface, which could lead to erroneous EDS measurements. In addition, EDS data for elements with less than <2 atom% are likely unreliable, including Mg, which had ~ 0.3 atom%.

Aragonite single crystals possess a significantly higher stiffness [41] and elastic modulus [42] along their c-axis. Accordingly, we used correlative Raman crystallography–nanoindentation to investigate whether variations in crystal orientation could be directly correlated to a location-specific nanomechanical response. Raman spectra from the basal and prism facets of monocrystal geological aragonite were measured and collected in 0° and 90° orientations using parallel and cross polarizations (Fig. 7A). By comparing the collected spectra and filtering them for the in-plane and out-plane bending peaks [43], we confirmed that the presence of the 707 cm^{-1} peak in parallel-polarized measurements denoted the basal facet of the crystal. In addition, we determined crystal orientations along the c-axis using the 274 cm^{-1} and 854 cm^{-1} peaks, based on parallel and polarized measurements, respectively. Lastly, we extracted confocal Raman maps by filtering based differences in revealed peak intensities (Fig. 7B).

Both polarized Raman spectroscopy and EBSD revealed comparable orientation data, such that crystals with the base angle oriented outward (Fig. 7C, upper right) corresponded with crystals with [100] and [001] (purple/red) directions perpendicular to the surface (Fig. 7D, upper right). Crystals with the base angle oriented outward had the highest Young's modulus and hardness in the mapped region (Fig. 7E). Despite variations in Young's modulus and hardness in the mapped region (Fig. 7E), this trend between nanomechanical properties and crystal orientation was weak, suggesting that aragonite crystals in this coral sample did not behave as a single crystal. Within the skeletal ultrastructure, the COC displayed lower Young's modulus and hardness than surrounding fibers (Fig. 7E). The COC was predominately surrounded by crystals with the [010] direction perpendicular to the surface (Fig. 7C & D), as was found surrounding COCs in surfaces 2 & 3 of the WLT sample (Fig. 3). EDS maps showed higher atom% Ca in the COC region (~21 atom% Ca) than the fibers (~16 atom% Ca) (Fig. 7F), which may be an analytical artifact.

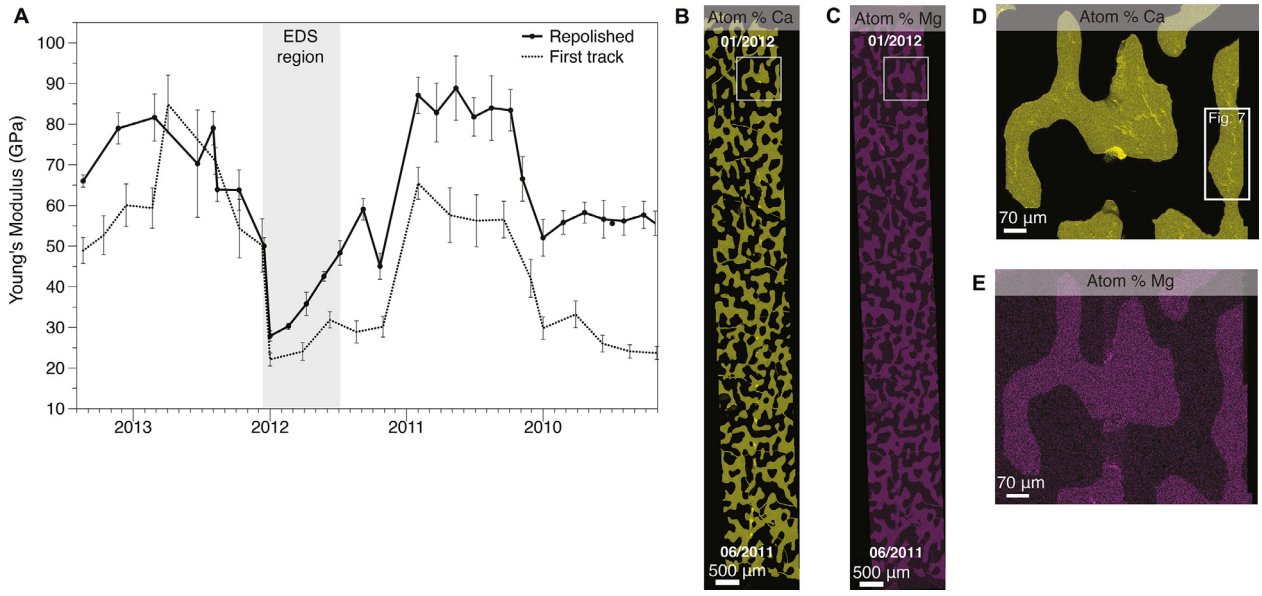

Fig. 6. (A) Repeated measurements along re-polished surface of the HBH Porites sample. (B) Energy-Dispersive X-ray Spectroscopy (EDS) was performed in the 2012-2011 region of the HBH core, due to its high variability in mechanical properties. Approximate dates are provided at the top and bottom of both images. The area indicated in (D) was used for high resolution nano-indentation mapping (see Fig. 7).

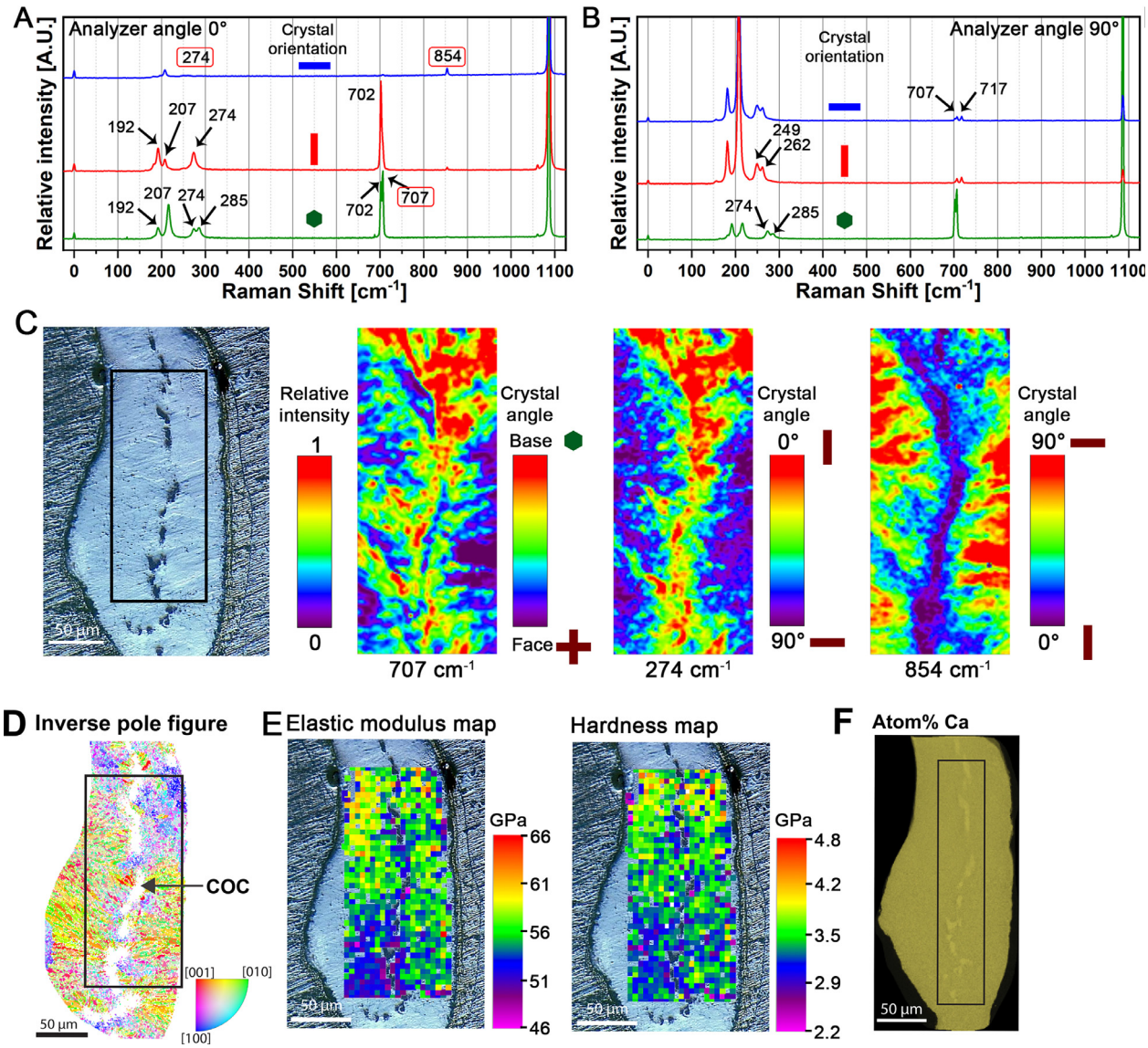

Fig. 7. Correlative Raman crystallography, EBSD, and nanoindentation on the longitudinal plane (surface 2) of the HBH *Porites* sample. Extracted Raman spectra from different crystallographic orientations of single crystal aragonite measured with (A) parallel polarization and (B) cross-polarization were used as a reference for orientation mapping of the coral sample. (C) FESEM micrograph of analyzed region (not-etched) and high-resolution Raman maps extracted from the coral sample filtered for 707 cm^{-1}, 274 cm^{-1}, and 854 cm^{-1} belong to CO_3 vibrational modes were used to investigate crystal orientations of the aragonite crystallites. These data were compared with (D) EBSD maps and used for correlative analysis of (E) elastic modulus and hardness nanoindentation maps with crystal orientation maps. Centers of calcification (COC) are non-indexed regions surrounded by indexed crystals. (F) EDS mapping of atom % Ca. (For interpretation of the references to colour in this figure legend, the reader is referred to the web version of this article.)

4. Discussion

In contrast with previous studies of coral skeletons, which have reported homogenous and isotropic skeletal properties in three scleractinian species [25,44], we observe anisotropy in *Porites* skeletons, marking the first time that mechanical anisotropy has been documented outside of bulk-scale measurements in corals [20]. In natural single-crystal form, anisotropy is well documented in aragonite, with a preferred orientation and along the c-axis and increased Young's modulus by a factor by approximately 1.8-fold [42,45,46]. As aragonite crystals are anisotropic, anisotropy was hypothesized to be a property of coral skeletons at crystallographic scales, and it has been observed in other aragonite biominerals [25,28,47]. Additionally, anisotropic elongation has been detected in coral skeletons by measuring aragonite unit cell parameters [30,48], and heterogeneous distributions of fiber bundles and growth regions are well documented [10,11].

Here, anisotropy was more pronounced at the scale of crystal bundles (5 µm tip radius) than at the nanoscale (140 nm tip radius), but overall, anisotropy was less pronounced than in single-crystal aragonite [42,46]. Together, these results suggest that packing and microarchitectural organization of the crystals affect skeletal mechanics at different scales. At the crystal bundle scale (microscale), slight differences in preferred crystal orientation, crystal packing, and grain size likely explain the observed anisotropy. Although reducing coral growth to three surfaces is a simplification of a complicated, three-dimensional biomineralization process, repeated measurements performed in the re-polished HBH sample demonstrate the robustness of these microscale mechanical trends (Fig. 6A), along with repeated microscale anisotropy measurements in core KRD. When comparing crystal orientation with mechanical properties at the nanoscale, we observed a correlative trend between Young's modulus and hardness and crystal orientation along the bases (perpendicular to the c-axis) (Fig. 7), yet this relation-

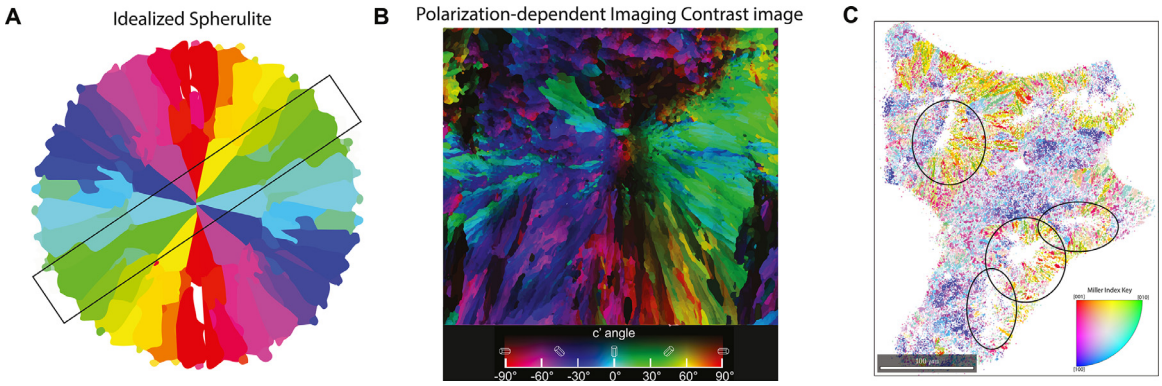

Fig. 8. (A) Idealized spherulite and (B) spherulitic growth pattern observed in Sun et al. [15] (copyright request number: 5250290496280). The rectangle in (A) represents how the transverse surface may capture spherulitic patterns. (C) EBSD crystal orientation mapping from surface 1 (transverse) with circles showing proposed spherulites.

ship was weaker than at the microscale. Differences between micromechanical and nanomechanical properties may be a result of biological nanogranular deposition. Aragonite crystals are formed by biologically driven nanoparticle agglomeration [1,13,15], which may not display a preferred orientation at the nanoscale, yet a preferred orientation could arise from crystal packing and organization. Across skeletal features, we also observed nanoscale trends between Young's modulus and crystal orientation within COCs, with COCs having lower mechanical properties and similar crystal orientations. As different species have different skeletal architecture with different COC and fiber dimensions [49,50], species-specific differences in micro- and nano-scale mechanical properties are also likely to occur.

Although we observed anisotropy, several similar studies have documented isotropy in coral skeletons [25,44]. Differences in anisotropy versus isotropy between studies may be a result of differences in coral species or sampling techniques. In contrast with existing nanoindentation studies of scleractinian coral, which use a sharp indenter [24,25,44], we document anisotropy using a blunt indenter, which produces a relatively smaller initial stress over a larger area, compressing a bundle of crystals. This difference in tip geometry does not appear to influence the validity of measured mechanical values, as evidenced by comparable values of nano- and micro-indentation measurements on the HBH coral using both a Berkovich indenter and a blunt indenter (Figs. 6 & 7). Instead, results from different tip geometries likely reflect the architectural organization of crystals at different scales.

In addition, differences in mechanical properties may also be species-specific, as massive and mounding corals, such as *Porites*, have lower compressive and tensile strength [19] than branching corals. Previously studied species using nanoindentation include the tropical branching coral *S. pistillata* [25], solitary Mediterranean corals *B. europaea* and *Leptopsammia pruvoti* [25], and the branching cold-water coral *Lophelia pertusa* [24]. Each coral species has unique corallite dimensions, and within the skeletal ultrastructure, different species contain different ratios of COCs to fibers [49,50], which could result in species-specific mechanical properties (Fig. 7E). Species from different environments have also been found to have different crystal structure anisotropy [30]. These observations suggest that different coral species may have intrinsically different mechanical properties at the nano- and micro-scales, due to differences in skeletal morphology, growth rate, and hierarchical architectures. Further studies should characterize micro- and nanomechanical properties across a wider range of scleractinian species and environments, particularly key reef building species in ecologically important regions.

Similar to previous orientation mapping studies on coral skeletons, aragonite crystals were grouped into bundles with the c-axis oriented radially from the COC [13,15,16,24,25]. Recent studies of crystal orientation have documented spherulitic growth across a range of scleractinian coral species, including *Porites lobata* [15]. Here, analysis between surfaces supports the spherulitic growth model, as we see different patterns surrounding COCs between transverse (surface 1) and longitudinal (surfaces 2 & 3) planes. COCs along surface 1 displayed spherulitic-like range of orientations, similar to growth patterns to that of an idealized spherulite (Fig. 8A–C). In contrast, along the longitudinal surfaces, crystal orientations surrounding the COCs were predominately along one plane, rather than opposing planes. Cutting through spherulites longitudinally may expose crystals with parallel orientations along COCs (Fig. 8A), resulting in COCs surrounded by crystals of similar orientations (Fig. 3).

In addition to orientation, grain size also differed slightly between transverse and longitudinal surfaces, with the transverse surface (surface 1) having larger grains. Grains may be larger from the transverse perspective, as more crystals are aligned with the coral's primary macroscale growth direction. In non-biogenic materials (e.g. ceramics, copper, diamond), numerous studies have observed that Young's modulus and hardness can increase with increasing grain size [51–53]; yet, this relationship does not always hold true, as an increase in grain boundaries (i.e. smaller grains) can also increase hardness and yield strength [54]. In biominerals, the relationship between grain size and mechanical properties is poorly studied; however, a correlation between hardness and grain size was also observed in parrotfish enamel [34].

Aside from grain size and crystal orientation, chemical composition and lattice defects are also known to alter material properties [27,29,55,56]. Defects cause local deformation of the crystal, essentially stretching or compressing ionic bonds creating atomic scale defects, known as dislocations. Due to the sharp gradient in Young's modulus in one of our Taiwan samples (Fig. 6), we hypothesized that a gradient in chemical composition would be detectable by EDS mapping. However, no difference was detected in the region analyzed. While EDS mapping in this study revealed an unusual trend, of the COC being more enriched in Ca and depleted in Mg, this result should be interpreted with caution as it may be an analytical artifact related to both polishing and the sensitivity of EDS analysis. COC regions appeared to have a negative relief in FESEM micrographs (non-etched) (Fig. 7C). Although etched FESEM micrographs (Fig. 1C–F) and Raman spectra (Fig. S1) show that the COC was not resin infilled, COC structures did not have a crystalline index in EBSD maps. Higher organic content and amorphous calcium carbonate in COCs may cause these regions to polish more readily than the surrounding fibers, impacting both EBSD indexing and EDS mapping. Higher Mg content in COCs is well documented, as these regions have the highest mineral growth rate [57–59] and

higher Mg incorporation into calcium carbonate is associated with higher mineral growth rates [60,61]. Previous studies show that Mg is typically 1.3- to 4-fold higher in the COC than the surrounding aragonite fibers [57–59] and may stabilize amorphous calcium carbonate during mineral formation [14,57,62]. Here, atom% Mg is likely unreliable due to its low concentration (∼ 0.3 atom% Mg) and the sensitivity of EDS analysis. Regarding the higher Ca content observed in COCs, which is well-within detection range of EDS, we hypothesize that this could be an analytical artifact associated with uneven polishing of the weaker, amorphous COC region. Future studies should combine mechanical measurements with more sensitive chemical mapping techniques, such as laser ablation inductively coupled plasma mass spectrometry (LA-ICP-MS) or ion microprobe analysis [57–59,61].

As *Porites* corals are likely to incur higher forces in the direction parallel to corallite growth, particularly from predation and environmental stimuli, anisotropy may provide the skeleton with a structural advantage. Here, we not only document anisotropy, but also propose that grain size and crystal orientation are likely to play a key role in controlling micromechanical properties. While these findings do not contradict recent mineralization models centered around spherulitic growth and robust micromechanical properties [15,16,24], they demonstrate *Porites* skeletons are not isotropic and that mechanical and crystallographic properties can vary within skeletons. This is consistent with both the anisotropic nature of aragonite [41], observations of aragonite crystals in coral [30], and coral growth models, which show that skeletal extension is spatially heterogeneous [10]. Understanding what drives differences in mechanical properties of coral skeletons not only improves our fundamental knowledge of coral biomineralization and geochemistry, but can also provide insight into the skeleton's ability to withstand environmental and anthropogenic forces, including grazing, micro- and macro-boring, destructive fishing, severe storms, and ocean acidification. Work coupling mechanical measurements with mineralogy and geochemistry [23] is critical in the context of climate change, as ocean acidification has been shown to change coral crystal structures and crystallite orientation [22,63,64] and increase bioerosion rates [65–67]. By incorporating micromechanical measurements into future studies, we can better understand and predict how changing environmental conditions may impact the integrity of coral skeletons and the ecosystem services they provide.

Declaration of Competing Interest

The authors declare that they have no conflict of interest.

Acknowledgments

Funding was provided by the National Research Foundation Singapore (NRF-RF2012-03 to NFG), Singapore Ministry of Education, Research Centers of Excellence initiative, the Marine Science R&D Programme (MSRDP-P03 and MSRDP-P29 to NFG and AM), and the American Museum of Natural History (NFG). This work represents EOS contribution number 465. Samples WLT and HBH were collected under permit #1020003149 from Kenting National Park. Sample KRD was collected under Proj. ID 2009/043 issued by the National Research Council of Thailand. Thank you to Gaëtan Spaey for assistance with image processing.

Supplementary material

Supplementary material associated with this article can be found, in the online version, at doi:10.1016/j.actbio.2022.08.012.

References

[1] T. Mass, A.J. Giuffre, C.-Y. Sun, C.A. Stifler, M.J. Frazier, M. Neder, N. Tamura, C.V. Stan, M.A. Marcus, P.U.P.A. Gilbert, Amorphous calcium carbonate particles form coral skeletons, PNAS 114 (37) (2017) E7670–E7678.
[2] A.L. Cohen, T.A. McConnaughey, Geochemical perspectives on coral mineralization, Rev. Mineral. Geochem. 54 (1) (2003) 151–187.
[3] F. Moberg, C. Folke, Ecological goods and services of coral reef ecosystems, Ecol. Econ. 29 (2) (1999) 215–233.
[4] J.A. Johnson, C.T. Perry, S.G. Smithers, K.M. Morgan, N. Santodomingo, K.G. Johnson, Palaeoecological records of coral community development on a turbid, nearshore reef complex: baselines for assessing ecological change, Coral Reefs 36 (3) (2017) 685–700.
[5] N.A.J. Graham, K.L. Nash, The importance of structural complexity in coral reef ecosystems, Coral Reefs 32 (2) (2012) 315–326.
[6] M.S. Pratchett, P. Munday, S. Wilson, N.A. Graham, J.E. Cinner, D.R. Bellwood, G.P. Jones, N.V. Polunin, T.R. McClanahan, Effects of climate-induced coral bleaching on coral-reef fishes, Oceanogr. Mar. Biol. 46 (2008) 251–296.
[7] S. Tambutté, M. Holcomb, C. Ferrier-Pagès, S. Reynaud, E. Tambutté, D. Zoccola, D. Allemand, Coral biomineralization: from the gene to the environment, J. Exp. Mar. Biol. Ecol. 408 (1–2) (2011) 58–78.
[8] J. Stolarski, Three-dimensional micro-and nanostructural characteristics of the scleractinian coral skeleton: a biocalcification proxy, Acta Palaeontol. Pol. 48 (2003) 497–530.
[9] C. Brahmi, I. Domart-Coulon, L. Rougée, D. Pyle, J. Stolarski, J. Mahoney, R. Richmond, G. Ostrander, A. Meibom, Pulsed 86Sr-labeling and nanosims imaging to study coral biomineralization at ultra-structural length scales, Coral Reefs 31 (2012) 741–752.
[10] I. Domart-Coulon, J. Stolarski, C. Brahmi, E. Gutner-Hoch, K. Janiszewska, A. Shemesh, A. Meibom, Simultaneous extension of both basic microstructural components in scleractinian coral skeleton during night and daytime, visualized by in situ ^{86}sr pulse labeling, J. Struct. Biol. 185 (2014) 79–88.
[11] F. Houlbreque, A. Meibom, J.-P. Cuif, J. Stolarski, Y. Marrocchi, C. Ferrier-Pagès, I. Domart-Coulon, R.B. Dunbar, Strontium-86 labeling experiments show spatially heterogeneous skeletal formation in the scleractinian coral *Porites porites*, Geophys. Res. Lett. 36 (2009) L04604.
[12] J. Stolarski, M. Mazur, Nanostructure of biogenic versus abiogenic calcium carbonate crystals, Acta Palaeontol. Pol. 50 (2005) 847–865.
[13] K. Benzerara, N. Menguy, M. Obst, J. Stolarski, M. Mazur, T. Tylisczak, G.E. Brown, A. Meibom, Study of the crystallographic architecture of corals at the nanoscale by scanning transmission X-ray microscopy and transmission electron microscopy, Ultramicroscopy 111 (8) (2011) 1268–1275.
[14] S. Von Euw, Q. Zhang, V. Manichev, N. Murali, J. Gross, L.C. Feldman, T. Gustafsson, C. Flach, R. Mendelsohn, P.G. Falkowski, Biological control of aragonite formation in stony corals, Science 356 (6341) (2017) 933–938.
[15] C.-Y. Sun, L. Gránásy, C.A. Stifler, T. Zaquin, R.V. Chopdekar, N. Tamura, J.C. Weaver, J.A.Y. Zhang, S. Goffredo, G. Falini, M.A. Marcus, T. Pusztai, V. Schoeppler, T. Mass, P.U.P.A. Gilbert, Crystal nucleation and growth of spherulites demonstrated by coral skeletons and phase-field simulations, Acta Biomater. (2020) 1–16.
[16] C.-Y. Sun, M.A. Marcus, M.J. Frazier, A.J. Giuffre, T. Mass, P.U.P.A. Gilbert, Spherulitic growth of coral skeletons and synthetic aragonite: nature's three--dimensional printing, ACS Nano 11 (7) (2017) 6612–6622.
[17] I. Coronado, M. Fine, F.R. Bosellini, J. Stolarski, Impact of ocean acidification on crystallographic vital effect of the coral skeleton, Nat. Commun. 10 (1) (2019) 1–9.
[18] J.S. Madin, S.R. Connolly, Ecological consequences of major hydrodynamic disturbances on coral reefs, Nature 444 (7118) (2006) 477–480.
[19] J.S. Madin, Mechanical limitations of reef corals during hydrodynamic disturbances, Coral Reefs 24 (4) (2005) 630–635.
[20] J.A. Chamberlain, Mechanical properties of coral skeleton: compressive strength and its adaptive significance, Paleobiology 4 (4) (1978) 419–435.
[21] T.E. Baldock, H. Karampour, R. Sleep, A. Vyltla, F. Albermani, A. Golshani, D.P. Callaghan, G. Roff, P.J. Mumby, Resilience of branching and massive corals to wave loading under sea level rise - a coupled computational fluid dynamics-structural analysis, Mar. Pollut. Bull. 86 (1–2) (2014) 91–101.
[22] S. Hennige, L. Wicks, N. Kamenos, G. Perna, H.S. Findlay, J.M. Roberts, Hidden impacts of ocean acidification to live and dead coral framework, Proc. R. Soc. B 282 (2015) 20150990.
[23] M.A. Moynihan, S. Amini, N.F. Goodkin, J.T.I. Tanzil, J.Q.I. Chua, G.N. Fabbro, T.-Y. Fan, D.N. Schmidt, A. Miserez, Environmental impact on the mechanical properties of *Porites* spp. corals, Coral Reefs (2021) 1–17.
[24] S.J. Hennige, U. Wolfram, L. Wickes, F. Murray, J.M. Roberts, N.A. Kamenos, S. Schofield, A. Groetsch, E.M. Spiesz, M.-E. Aubin-Tam, P.J. Etnoyer, Crumbling reefs and cold-water coral habitat loss in a future ocean: evidence of 'Coral-porosis' as an indicator of habitat integrity, Front. Mar. Sci. 7 (2020) 668.
[25] L. Pasquini, A. Molinari, P. Fantazzini, Y. Dauphen, J.P. Cuif, O. Levy, Z. Dubinsky, E. Caroselli, F. Prada, S. Goffredo, M. Di Giosia, M. Reggi, G. Falini, Isotropic microscale mechanical properties of coral skeletons, J. R. Soc. Interface 12 (106) (2015) 20150168.
[26] A. Carrasco-Pena, M. Omer, B. Masa, Z. Shepard, T. Scofield, S. Bhattacharya, N. Orlovskaya, B.E. Collins, S.N. Yarmolenko, J. Sankar, et al., Mechanical properties, spectral vibrational response, and flow-field analysis of the aragonite skeleton of the staghorn coral (*Acropora cervicornis*), Coral Reefs 39 (2020) 1779–1792.

[27] B. Pokroy, A.N. Fitch, P.L. Lee, J.P. Quintana, E.N. Caspi, E. Zolotoyabko, Anisotropic lattice distortions in the mollusk-made aragonite: a widespread phenomenon, J. Struct. Biol. 153 (2) (2006) 145–150.
[28] A. Lin, M.A. Meyers, Growth and structure in abalone shell, Mater. Sci. Eng. A 390 (1–2) (2005) 27–41.
[29] E.N. Caspi, B. Pokroy, P.L. Lee, J.P. Quintana, E. Zolotoyabko, On the structure of aragonite, Acta Crystallogr. B61 (2) (2005) 129–132.
[30] G.A. Farfan, A. Apprill, A. Cohen, T.M. DeCarlo, J.E. Post, R.G. Waller, C.M. Hansel, Crystallographic and chemical signatures in coral skeletal aragonite, Coral Reefs 41 (2022) 19–34.
[31] M. Cusack, J. England, P. Dalbeck, A.W. Tudhope, A.E. Fallick, N. Allison, Electron backscatter diffraction (EBSD) as a tool for detection of coral diagenesis, Coral Reefs 27 (4) (2008) 905–911.
[32] V. Mouchi, P. Vonlanthen, E.P. Verrecchia, Q.G. Crowley, Multi-scale crystallographic ordering in the cold-water coral *Lophelia pertusa*, Sci. Rep. 7 (1) (2017) 1–10.
[33] J. Vernon, Corals of the World, Australian Institute of Marine Science, Townsville, Australia, 2000.
[34] M.A. Marcus, S. Amini, C.A. Stifler, C.-Y. Sun, N. Tamura, H.A. Bechtel, D.Y. Parkinson, H.S. Barnard, X.X.X. Zhang, J.Q.I. Chua, A. Miserez, P.U.P.A. Gilbert, Parrotfish teeth: stiff biominerals whose microstructure makes them tough and abrasion-resistant to bite stony corals, ACS Nano 11 (12) (2016) 11856–11865.
[35] W.C. Oliver, G.M. Pharr, Measurement of hardness and elastic modulus by instrumented indentation: advances in understanding and refinements to methodology, J. Mater. Res. 19 (1) (2004) 3–20.
[36] M. Wall, G. Nehrke, Reconstructing skeletal fiber arrangement and growth mode in the coral *Porites lutea* (Cnidaria, Scleractinia): a confocal Raman microscopy study, Biogeosciences 9 (11) (2012) 4885–4895.
[37] J.P. Cuif, Y. Dauphin, Microstructural and physico-chemical characterization of centers of calcification in septa of some recent scleractinian corals, Palaontol. Z. 72 (3–4) (1998) 257–269.
[38] F. Bachmann, R. Hielscher, H. Schaeben, Texture analysis with mtex–free and open source software toolbox, in: Solid State Phenomena, vol. 160, Trans. Tech. Publ., 2010, pp. 63–68.
[39] S. Amini, H. Razi, R. Seidel, D. Werner, W.T. White, J.C. Weaver, M.N. Dean, P. Fratzl, Shape-preserving erosion controlled by the graded microarchitecture of shark tooth enameloid, Nat. Commun. 11 (1) (2020) 1–11.
[40] R Core Team, R: A language and environment for statistical computing, R Foundation for Statistical Computing, Vienna, Austria, 2019. https://www.R-project.org/.
[41] L.-g. Liu, C.-c. Chen, C.–C. Lin, Y.-j. Yang, Elasticity of single-crystal aragonite by Brillouin spectroscopy, Phys. Chem. Miner. 32 (2) (2005) 97–102.
[42] F. Barthelat, H. Espinosa, Elastic properties of nacre aragonite tablets, in: Proceedings of the SEM Annual Conference and Exposition on Experimental and Applied Mechanics, 2003. Charlotte, NC, Session 68, Paper 187, USA
[43] G. Farfan, C. Zhou, J. Valley, I. Orland, Coupling mineralogy and oxygen isotopes to seasonal environmental shifts recorded in modern freshwater pearl nacre from Kentucky Lake, Geochem. Geophys. 22 (2021) e2021GC009995.
[44] S. Goffredo, A. Mancuso, E. Caroselli, F. Prada, Z. Dubinsky, G. Falini, O. Levy, P. Fantazzini, L. Pasquini, Skeletal mechanical properties of Mediterranean corals along a wide latitudinal gradient, Coral Reefs 34 (1) (2014) 121–132.
[45] L.-g. Liu, C.-c. Chen, C.-C. Lin, Y.-j. Yang, Elasticity of single-crystal aragonite by Brillouin spectroscopy, Phys. Chem. Miner. 32 (2) (2005) 97–102.
[46] M. Levy, H. Bass, R. Stern, Handbook of Elastic Properties of Solids, Liquids, and Gases, Academic press, 2000.
[47] C. Kearney, Z. Zhao, B.J.F. Bruet, R. Radovitzky, M.C. Boyce, C. Ortiz, Nanoscale anisotropic plastic deformation in single crystal aragonite, PRL 96 (2006) 255505.
[48] J. Stolarski, R. Przeniosło, M. Mazur, M. Brunelli, High-resolution synchrotron radiation studies on natural and thermally annealed scleractinian coral biominerals, J. Appl. Crystallogr. 40 (1) (2007) 2–9.
[49] J.-P. Cuif, G. Lecointre, C. Perrin, A. Tillier, S. Tillier, Patterns of septal biomineralization in Scleractinia compared with their 28S rRNA phylogeny: a dual approach for a new taxonomic framework, Zool. Scr. 32 (2003) 459–473.
[50] J. Stolarski, M.V. Kitahara, D.J. Miller, S.D. Cairns, M. Mazur, A. Meibom, The ancient evolutionary origins of Scleractinia revealed by azooxanthellate corals, BMC Evol. Biol. 11 (2011) 1–11.
[51] C. Huang, X. Peng, B. Yang, S. Weng, Y. Zhao, T. Fu, Grain size dependence of tensile properties in nanocrystalline diamond, Comput. Mater. Sci. 157 (2019) 67–74.
[52] K. Zhou, B. Liu, Y. Yao, K. Zhong, Effects of grain size and shape on mechanical properties of nanocrystalline copper investigated by molecular dynamics, Mater. Sci. Eng. A 615 (C) (2014) 92–97.
[53] M. Trunec, Effect of grain size on mechanical properties of 3Y-TZP ceramics, Ceram.-Silik. 52 (2008) 165–171.
[54] M.A. Meyers, A. Mishra, D.J. Benson, Mechanical properties of nanocrystalline materials, Prog. Mater. Sci. 51 (4) (2006) 427–556.
[55] Y.-Y. Kim, J.D. Carloni, B. Demarchi, D. Sparks, D.G. Reid, M.E. Kunitake, C.C. Tang, M.J. Duer, C.L. Freeman, B. Pokroy, K. Penkman, J.H. Harding, L.A. Estroff, S.P. Baker, F.C. Meldrum, Tuning hardness in calcite by incorporation of amino acids, Nat. Mater. 15 (8) (2016) 903–910.
[56] Y. Ma, S.R. Cohen, L. Addadi, S. Weiner, Sea urchin tooth design: an "all-calcite" polycrystalline reinforced fiber composite for grinding rocks, Adv. Mater. 20 (8) (2008) 1555–1559.
[57] A. Meibom, J.-P. Cuif, F. Hillion, B.R. Constantz, A. Juillet-Leclerc, Y. Dauphin, T. Watanabe, R.B. Dunbar, Distribution of magnesium in coral skeleton, Geophys. Res. Lett. 31 (23) (2004) L23306.
[58] A.C. Gagnon, J.F. Adkins, D.P. Fernandez, L.F. Robinson, Sr/Ca and Mg/Ca vital effects correlated with skeletal architecture in a scleractinian deep-sea coral and the role of rayleigh fractionation, EPSL 261 (2007) 280–295.
[59] M. Holcomb, A.L. Cohen, R.I. Gabitov, J.L. Hutter, Compositional and morphological features of aragonite precipitated experimentally from seawater and biogenically by corals, Geochim. Cosmochim. Acta 73 (14) (2009) 4166–4179.
[60] V. Mavromatis, J.-M. Brazier, K.E. Goetschl, Controls of temperature and mineral growth rate on Mg incorporation in aragonite, Geochim. Cosmochim. Acta 317 (2022) 53–64.
[61] R. Gabitov, G. Gaetani, E. Watson, A. Cohen, H. Ehrlich, Experimental determination of growth rate effect on U^{6+} and Mg^{2+} partitioning between aragonite and fluid at elevated u^{6+} concentration, Geochim. Cosmochim. Acta 72 (16) (2008) 4058–4068.
[62] A. Akiva, M. Neder, K. Kahil, R. Gavriel, I. Pinkas, G. Goobes, T. Mass, Minerals in the pre-settled coral *Stylophora pistillata* crystallize via protein and ion changes, Nat. Commun. 9 (1) (2018) 1880.
[63] G.A. Farfan, E.E. Cordes, R.G. Waller, T.M. DeCarlo, C.M. Hansel, Mineralogy of deep-sea coral aragonites as a function of aragonite saturation state, Front. Mar. Sci. 5 (2018) 473.
[64] I. Coronado, M. Fine, F.R. Bosellini, J. Stolarski, Impact of ocean acidification on crystallographic vital effect of the coral skeleton, Nat. Commun. 10 (2019) 1–9.
[65] C.H. Schönberg, J.K. Fang, M. Carreiro-Silva, A. Tribollet, M. Wisshak, Bioerosion: the other ocean acidification problem, ICES J. Mar. Sci. 74 (2017) 895–925.
[66] I.C. Enochs, D.P. Manzello, G. Kolodziej, S.H. Noonan, L. Valentino, K.E. Fabricius, Enhanced macroboring and depressed calcification drive net dissolution at high-CO_2 coral reefs, Proc. Royal Soc. B 283 (2016) 20161742.
[67] A. Tribollet, C. Godinot, M. Atkinson, C. Langdon, Effects of elevated pCO_2 on dissolution of coral carbonates by microbial euendoliths, Global Biogeochem. Cycles 23 (2009).